Ore Geology Reviews 131 (2021) 104030

Contents lists available at ScienceDirect

Ore Geology Reviews

journal homepage: www.elsevier.com/locate/oregeorev

Fluid-rock interaction of the early Cambrian black shale in the South China Block: Implications for low-temperature mineralisation

Yonglei Zhang [a], Dan-Ping Yan [a,*], Jian-Feng Gao [b], Liang Qiu [a], Minghua Ren [c], Yue Zhang [a], Baifa Zhang [d], Dongcan Xu [a]

[a] The State Key Laboratory of Geological Processes and Mineral Resources, China University of Geosciences, Beijing 100083, China
[b] Institute of Geochemistry, Chinese Academy of Sciences, Guiyang, 550002, China
[c] Department of Geosciences, University of Nevada Las Vegas, Las Vegas, NV 89154-4010, USA
[d] Guangzhou Institute of Geochemistry, Chinese Academy of Science, Guangzhou, 510640, China

ARTICLE INFO

Keywords:
Water/rock interaction
Hydrothermal experiment
Leaching
Pyrite
Niutitang Formation
Simulation

ABSTRACT

Chalcophile elements hosted by black shales of the Lower Cambrian Niutitang Formation, South China Block, contribute to low-temperature mineralisation in southwest China. To study the mobilisation and migration of ore-forming elements, hydrothermal experiments were performed to simulate leaching of Au, As, Sb and Ag from an Au-rich black shale from the Kaiyang Phosphate Mine (KYPM), China. The experiments were designed to simulate low-temperature mineralisation at 150 °C, with solvent concentrations of ~5%, durations of 15 d and 30 d, and water/rock mass ratios of 13:1 and 26:1. Reagent-grade NaCl, $NaHCO_3$ and Na_2S were used to provide the common anions found in hydrothermal systems. The results show that solutions containing Cl^- ions in oxidised acidic systems leached Au most effectively. Weakly alkaline systems containing HCO_3^- ions leached Au less effectively. Solutions containing HS^- ions did not leach Au effectively, and Au precipitated within the HS^--bearing system. The results for Ag were similar to those for Au, and Ag-leaching was most effective in the oxidised acidic system containing Cl^- ions. As-leaching does not occur in the Cl^--bearing system, but As is leached effectively by HS^--bearing and HCO_3^--bearing solutions. Sb was not leached by our experiments. Oxidised fluids produced by deep-sourced magma during the Indosinian and Yanshanian tectonic events infiltrated black shales affected by extensional deformation through faults, joints and fractures. Fluid–rock interaction leached a range of elements in these structural settings. These experiments provide insights into migration of chalcophile elements, particularly Au and Ag, and the source of large-scale low-temperature mineralisation within the South China Block.

1. Introduction

Black shales are fine-grained, organic-rich, sedimentary rocks formed in marine environments, and typically contain pyrite and siderite (Gao et al., 1997; Kwong et al., 2009; Matlakowska and Sklodowska, 2011). Black shales are commonly enriched in a range of trace elements of economic interest, such as Cd, Ni, As, Mo, V, U, Au, Ag, Sb and PGEs. These trace elements can be enriched by factors of 10^5 to 10^6 relative to present-day seawater (Falk et al., 2006; Hu et al., 2007; Yu et al., 2014; Liu et al., 2017). However, most black shales worldwide have little economic value due to the low abundance of valuable elements.

Black shales enriched in ore-forming elements can contribute to epigenetic mineralisation. For example, large amounts of anhydrite, gypsum and barite formed from hydrothermal fluids that interacted with felsic rocks during late smectite alteration within the Kuroko ore deposits (Ogawa et al., 2005). In recent years, interest in leaching and extraction of base and noble metals from sub-economic black shales has increased, and laboratory and pilot-scale research projects using biological or chemical leaching agents have been performed (Anjum et al., 2010; Li et al., 2010; Watling et al., 2017). However, leaching processes and the amounts of elements that can be leached from black shales in natural environments remain poorly understood.

The early Cambrian black shales of the South China Block form one of the largest black shale exposures worldwide. They extend for up to 1600 km and strike ENE–WSW (Mao et al., 2002; Hu et al., 2007; Yu

* Corresponding author at: The State Key Laboratory of Geological Processes and Mineral Resources, China University of Geosciences, Beijing 100083, China.
E-mail address: yandp@cugb.edu.cn (D.-P. Yan).

https://doi.org/10.1016/j.oregeorev.2021.104030
Received 7 July 2020; Received in revised form 18 January 2021; Accepted 22 January 2021
Available online 2 February 2021

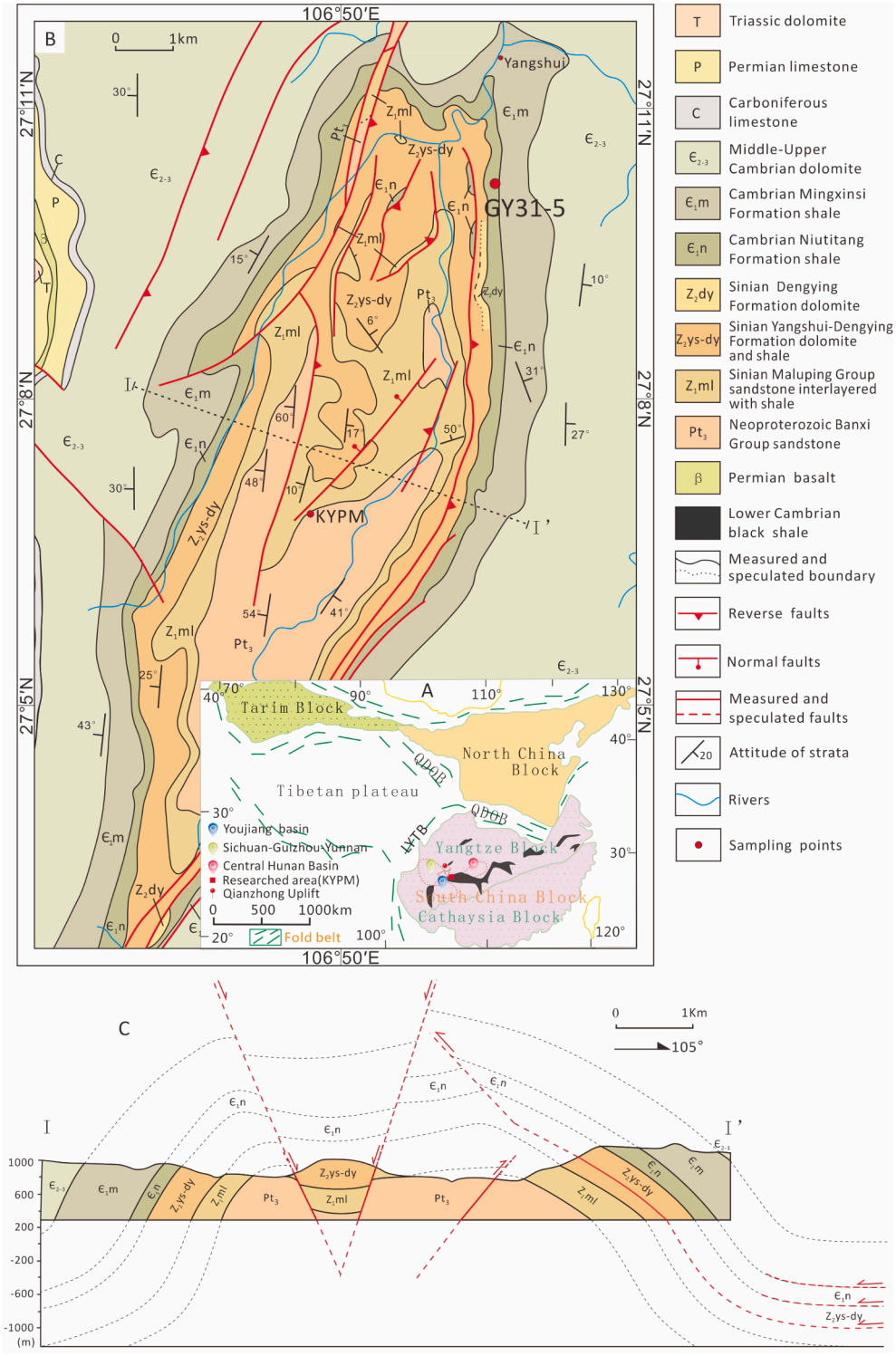

Fig. 1. (A) Tectonic framework of the Yangtze Block and adjacent continents (modified after Yan et al., 2009). (B) Geological map of Yangshui anticline (modified after BGMRGZ (1987)). (C) Cross-section I-I' through Yangshui anticline. Abbreviations: KYPM, Kaiyang Phosphate Mine; LYTB, Longmenshan-Yanyuan Thrust Belt; QDOB, Qingling-Dabie Orogenic Belt.

et al., 2012; Fig. 1A). The geochemistry, geological setting, age and source of mineralisation, and petrogenesis of black shales of the South China Block have been studied extensively (Mao, 2001; Chen et al., 2003; Yang et al., 2004, 2007; Xu et al., 2011, 2013; Wang et al., 2012; Lehmann et al., 2016; Yin et al., 2017). Zhang et al. (2016) described the stratigraphy of black shales at the Kaiyang Phosphate Mine (KYPM), China, and studied the behaviour of elements of economic interest (i.e., Au, Ag, As, Sb) at low temperature to constrain the metal source. However, in spite of extensive research on the KYPM black shales, important questions remain unresolved. These include the geodynamic setting of mineralisation, metal sources and the role of regional structures in mineralisation. Moreover, the processes that mobilised and transported ore-forming elements, particularly Au and Ag, remain unclear.

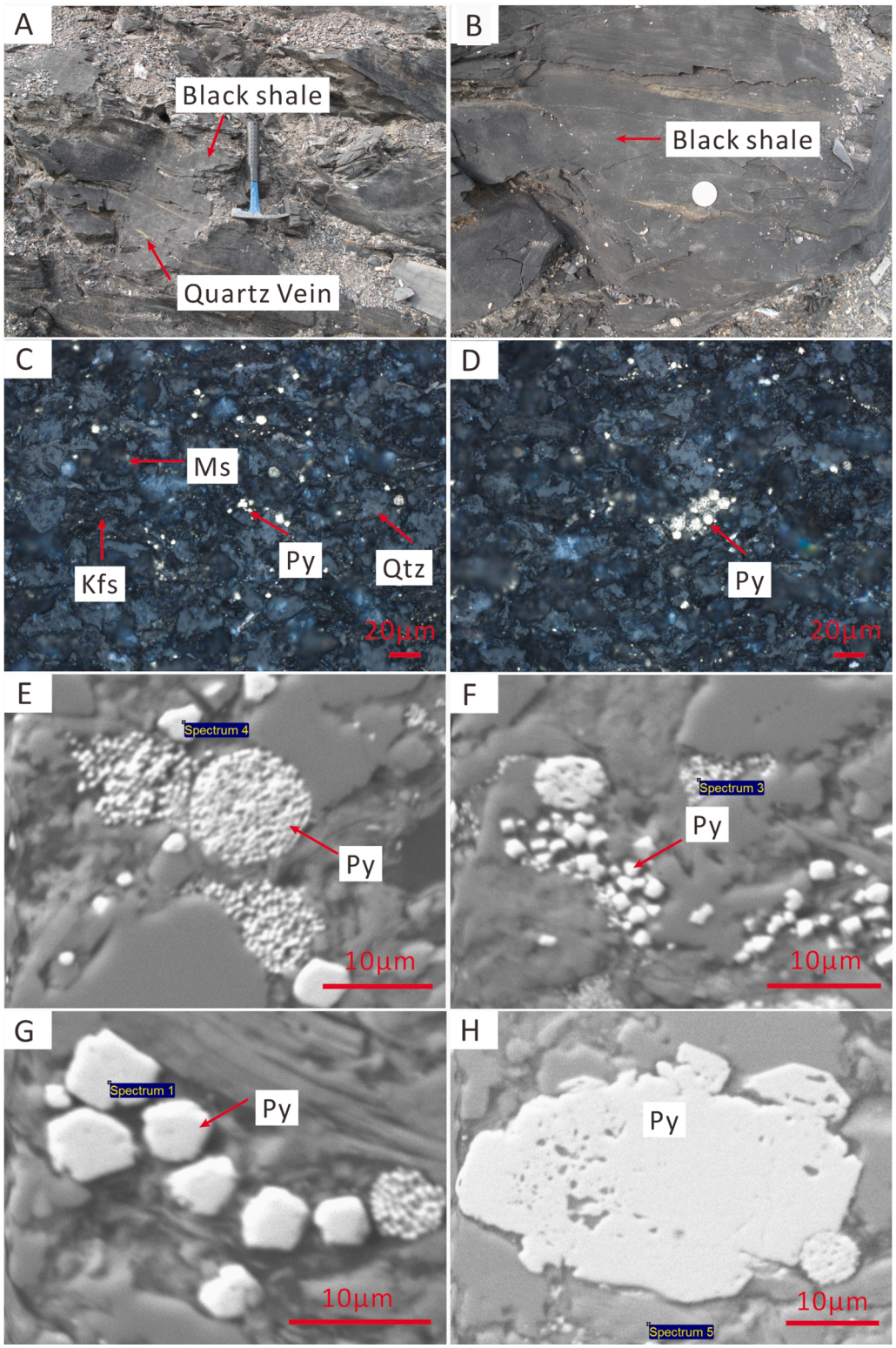

Fig. 2. (A) and (B) Representative field photographs of black shale enriched in quartz veins showing hydrothermal activity; (C) and (D) Reflected light photomicrographs of black shale; (E)-(H) SEM images of pyrite in the black shale. Mineral abbreviations: Py, pyrite; Qtz, quartz; Kfs, K-feldspar; Ms, Muscovite.

This study focuses on mobilisation and transport of Au, Ag, As and Sb hosted by black shales. The KYPM exposes a continuous profile of Lower Cambrian black shale. Many gold deposits have been discovered in the low-temperature metallogenic province of South China, in which the KYPM is hosted by Au-riched black shales with the highest Au concentration reach up to 0.344 ppm.

2. Geological background

Low-temperature mineralisation within the South China Block occurs over an area of 5×10^5 km^2, mainly within the southwest Yangtze Block, including the Youjiang Basin, the Central Hunan Basin and the Sichuan–Yunnan–Guizhou region (Fig. 1A). Carlin-type gold deposits

and other large and giant low-temperature polymetallic deposits are common in this area (Hu and Zhou, 2012).

The South China Block formed during the Neoproterozoic by amalgamation of the Cathaysia and Yangtze Blocks along the Jiangnan Orogenic Belt (Fig. 1A; Wang et al., 2013; Qiu et al., 2017, 2019). The South China Block is separated from the North China Block to the north by the E–W-striking Qinling–Dabie Orogenic Belt (QDOB; Liu et al., 2005; Zhang et al., 2006), and from the Songpan–Ganze Orogenic Belt to the west by the Cenozoic Longmenshan–Yanyuan Thrust Belt (LYTB; Qi and Zhou, 2008; Yan et al., 2008, 2011; Zhou et al., 2008). The Yangtze Block consists mainly of Proterozoic basement, which was folded and metamorphosed to greenschist to lower amphibolite facies (Robinson and Zhou, 2008; Wang et al., 2012). The Yangtze Block is covered by shallow-marine strata that were folded during the Palaeozoic and the early Mesozoic, and middle–late Mesozoic and Cenozoic continental clastic sequences (Yan et al., 2006).

In the Yangtze Block, the effects of Mesozoic Indosinian and Yanshanian tectonism are superimposed on E–W-oriented early Palaeozoic Caledonian Qianzhong uplift (Deng et al., 2010). The E–W-striking fault and fold system was overprinted by N–S-striking and NE–SW-striking fold–fault systems (Liu et al., 2005; Yan et al., 2009; Deng et al., 2010). The NE–SW-striking Yangshui anticline is a typical fold formed by early Palaeozoic Qianzhong uplift (Fig. 1A).

2.1. Geochemistry of low-temperature mineralisation within the Yangtze Block

There are three main areas of mineralisation within the southwestern Yangtze Block (Hu and Zhou, 2012; Zhou et al., 2014). The Sichuan–Yunnan–Guizhou region is enriched in Pb and Zn, the Youjiang Basin is enriched in Au, Sb, As and Hg, and the Central Hunan Basin is enriched mainly in Au and Sb. Low-temperature mineralisation is widespread in Precambrian to Triassic strata, and different elements are enriched in different units and lithologies. Au occurs mainly in Triassic argillaceous limestone (Hu et al., 2002), and Sb occurs mainly in Devonian carbonates and calcareous clastic rocks (Hu et al., 2007). In contrast, Hg occurs mainly in Cambrian rocks and Pb and Zn occur mainly within Neoproterozoic, Carboniferous and Permian dolomite and dolomitic limestone (Hu et al., 2007; Zhou et al., 2014). Carlin-type Au deposits are also commonly enriched in As, Sb, Hg, Tl, Ba and other elements. The Pb–Zn deposits are also enriched in Ag, Ge and Cd (Hu et al., 2002; Liu et al., 2007; Su et al., 2009). Reserves of Sb within the southwestern Yangtze Block account for 50% of global reserves, and Au and Hg reserves form 10% and 80% of Chinese reserves, respectively (Tu, 2002; Zhao and Tu, 2003). Moreover, this area is one of the most important Pb–Zn-producing regions in China. Gold, As, Sb and Ag are the main ore-forming elements found within the low-temperature mineralisation. The conditions of low-temperature mineralisation have been defined differently by several authors, but temperatures are typically agreed to be 150–250 °C (Roedder, 1984; Li, 1999; Hu et al., 2016). Other temperature classifications are considered arbitrary, and there is a continuum between medium–low temperature and high–low temperature metamorphism.

2.2. Geology of the Yangshui anticline

Black shale samples were collected from the Yangshui anticline, which exposes black shale of the Niutitang Formation at the KYPM, within the Yangtze Block (Fig. 1B). The Yangshui anticline has a NNE-plunging axis that extends over ~30 km. It is spindle-shaped and ~8 km-wide (Fig. 1B). The anticline is asymmetric, and the fold axial plane dips at ~ 60° to the west (Fig. 1B and C). Strata on the western limb typically dip at 15°–60° to the west, and strata on the eastern limb typically dip at 20°–40° to the east. The anticline is modified by thrust faults, which formed upright and overturned strata, and is cut by younger normal faults (Fig. 1B and C; Zhang et al. 2016). The main thrust faults are NNE–SSW-striking, cut the eastern limb of the anticline and are associated with typical fault-related folds (Fig. 1C; Zhang et al., 2016). High-angle normal faults, striking NNE–SSW and dipping E or W at 50°–80° cut the anticline and form horst and graben structures. Minor strike-slip faults striking WNW–ENE cut the anticline.

The Neoproterozoic Banxi Group forms the core of the Yangshui anticline, and Sinian and Cambrian strata form the limbs. Ordovician, Silurian and Devonian sedimentary rocks are separated from Carboniferous rocks adjacent to the Yangshui anticline by an unconformity formed by Caledonian tectonic activity (Song et al., 2017). Permian and Triassic sediments occur on the limbs of the anticline outside the study area (Fig. 1B).

Table 1
Trace elements of the sample GY31-5.

Sample no.	Au	As	Ag	Sb	Zn	Te	Pb
GY31-5 (ppm)	0.3443	46	2.16	0	74	0.19	20.8

3. Sampling and analytical methods

3.1. Sampling

Black shale sample GY31-5 (Fig. 2A and B) was collected and the whole-rock composition was measured (Table 1). The sample was collected from the Lower Cambrian Niutitang Formation on the eastern limb of the Yangshui anticline. Quartz veins within the black shale record hydrothermal activity in the past (Fig. 2A). Pyrite, which is the only sulfide in this black shale, was analysed by petrographic microscope (Fig. 2C and D) and scanning electron microscope (SEM; Fig. 2E-H). Pyrite has a characteristic yellowish-white metallic lustre and occurs as irregular single grains and grain aggregates under reflected light microscope. Electron probe microanalysis (EPMA) and SEM results indicate the major minerals are pyrite, quartz, K-feldspar, albite, muscovite with small amounts of apatite, sphene, and dolomite. The single pyrite grain is mainly subhedral, and the aggregates form framboids, a few micrometres to tens of micrometres in size. The sample was crushed, ground and sieved and the less-than-200 mesh portions was used for the hydrothermal experiments.

3.2. Trace element contents

Trace element contents were measured by inductively coupled plasma–mass spectroscopy (ICP–MS) on an Agilent 7700X instrument at Nanjing FocuMS Technology Co. Ltd, Jiangsu province, China. For As, Ag, Sb, Zn, Te and Pb, about 50 mg of sample was weighed accurately and dissolved in HF (1.0 mL) + HNO_3 (0.6 mL) in high-pressure PTFE bombs. The bombs were steel-jacketed and placed in an oven at 195 °C for 48 h. The solution was removed from the oven, dried to remove HF, a Rh internal standard solution was added, and the resulting solution was reacted with 5 mL of 40% HNO_3 at 140 °C for 5 h. After that, the sample was diluted by a factor of 2000, and analysed by ICP–MS. Repeated analysis of standards shows that the analytical precision was better than 5%. For Au, 5.00 g of sample (200 mesh) was weighed accurately and heated at 700 °C for 1 h. The sample was mixed with 40.0 mL diluted (1:1) aqua regia by shaking and heating, and was then diluted to 75.0 mL after 1 h. Au was adsorbed by polyfoam. The polyfoam was taken out and heated with 10.0 mL 0.2% thiourea for 30 min to release Au. Ir (1000 ppb, 200 μL) was added as internal standard. The precision was better than 10%.

3.3. Electron probe microanalysis

Mineral compositions were measured by electron probe microanalysis (EPMA) on a JEOL 8900 Superprobe at the Electron Microscope Image Laboratory, University of Nevada, Las Vegas, USA. The

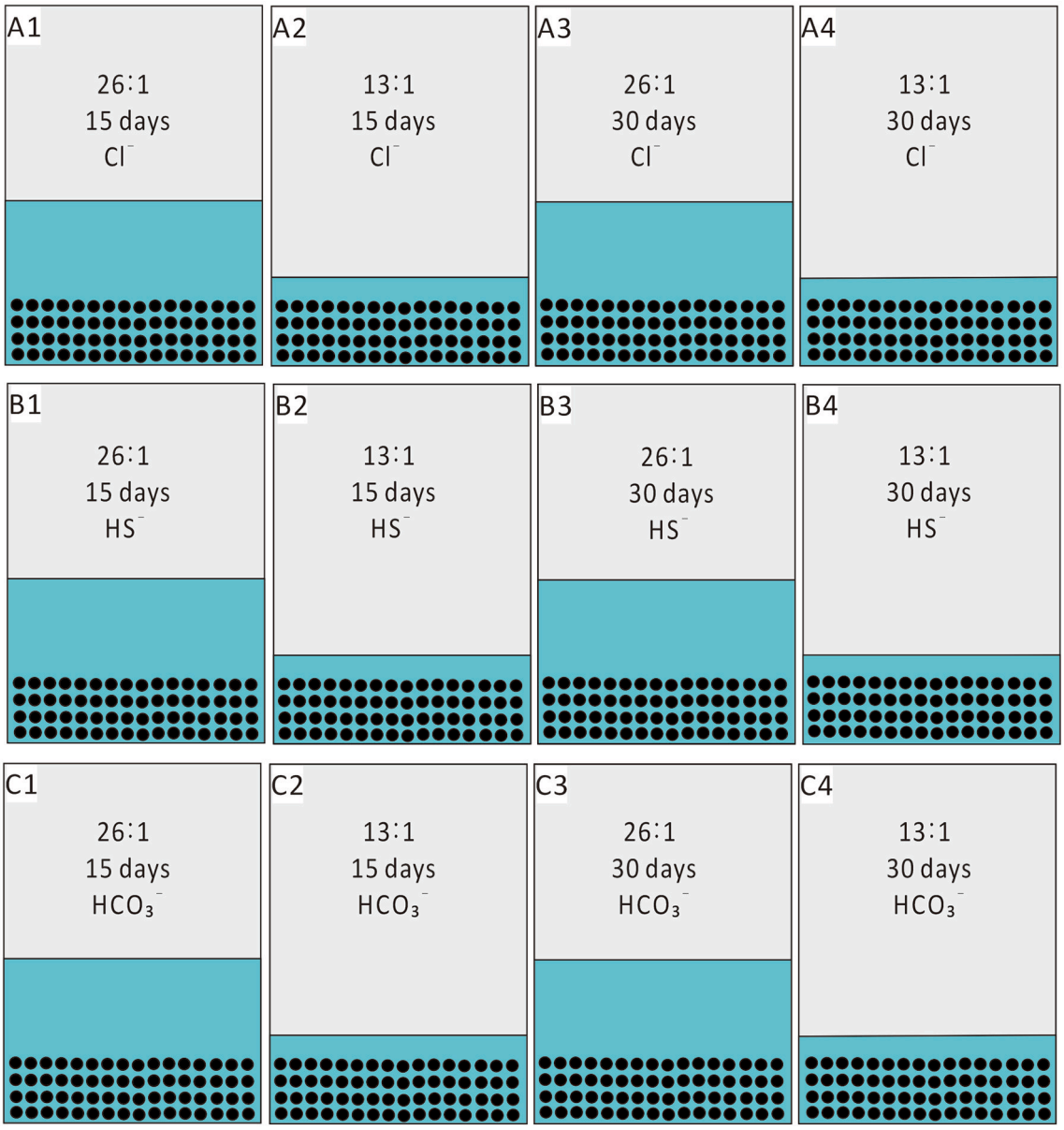

Fig. 3. Simulated condition of hydrothermal experiments. Group A includes A1, A2, A3, A4; Group B includes B1, B2, B3, B4; Group C includes C1, C2, C3, C4.

microprobe is equipped with four wavelength dispersive detectors and an Oxford energy dispersive spectroscopy (EDS) detector. The laboratory has a comprehensive set of oxide, carbonate, sulphide, sulphate and native element standards that cover most of the periodic table. Analysis was performed at 20 kV accelerating voltage, 10 nA beam current, 10 μm spot, and 30 s peak counting time. Au was measured in trace mode, with 200 s peak counting time and 50 s background counting time. The detection limit for Au is 130 to 140 ppm. The Au EPMA data were compared with laser ablation (LA)–ICP–MS Au data obtained at the United States Geological Survey (USGS) laboratory on the same samples for pyrite grains with Au contents >200 ppm. The EPMA and LA–ICP–MS data are in good agreement. The use of Au metal as a standard is a common practice in trace element analysis by EPMA for the following reasons: (1) No natural minerals have a constant Au content that can be used as an EPMA Au standard. (2) In trace element analysis by EPMA analysis, background selection is more challenging than standard selection. This method is also applied in monazite U–Th–Pb geochronology, where U- and Th- oxides are used as U and Th standards because U–Th phosphates are not available for use as U–Th standards.

3.4. Hydrothermal experiments

In this study, the experimental conditions were chosen primarily to simulate ore-formation. Carlin-type gold deposits, Nevada, USA, formed from low salinity (mostly ≤6 wt% NaCl eq.), CO_2-bearing (<4 mol.%) non-boiling fluids at 180–240 °C (Muntean et al., 2011). Coexisting illite and kaolinite reflect acidic conditions and ore formation at depths of >3.0 km. Aqueous fluid inclusions from Carlin-type gold deposits in China contain CO_2, have relatively low homogenisation temperatures (150–250 °C) and medium salinities (2–8 wt% NaCl eq.), and reflect pressures of 10^5–330 × 10^5 Pa, indicating depths of >1.0–3.0 km, assuming hydrostatic conditions (Hu et al., 2002; Su et al., 2009; Muntean et al., 2011; Gu et al., 2012; Liu et al., 2015). Wu et al. (2016) studied low-temperature, low-salinity fluid inclusions to investigate ore-forming fluids related to a Carlin-type ore field within the southwestern Yangtze Block. Barnes (1979) argued that the most common hydrothermal fluids contain 1.0 mol. kg^{-1} Cl^-, 0.1 mol. kg^{-1} HCO_3^-, 0.1 mol. kg^{-1} sulphur compound ions and 0.01 mol. kg^{-1} ammonia, corresponding to 5%–8% mass ratio of dissolved solids, assuming that $Na^{\pm}$ is

Table 2
The pH value of solutions before and after the experiments.

pH	A1	A2	A3	A4	B1	B2	B3	B4	C1	C2	C3	C4
1	4.13	4.10	3.92	3.96	8.65	8.61	8.58	8.63	9.18	9.20	9.19	9.21
2	4.95	5.1	5.01	5.23	8.11	8.03	7.82	8.01	8.19	8.22	8.32	8.09

Note. "1″ is the pH before the experiment; "2" is the pH after the experiment.

the dominant cation within the hydrothermal system.

Experimental conditions for the hydrothermal system simulated in the present study are based on the fluid properties summarised above (e.g., Barnes, 1979; Hu et al., 2002, 2016; Su et al., 2009; Muntean et al., 2011; Wu et al., 2016), at temperature of 150 °C, solute concentrations of ~ 5%, durations (D) of 15 or 30 d and water/rock (W/R) mass ratios of ~13:1 or 26:1. These W/R values represent a relatively closed system with less hydrothermal recharge and a relatively open system with more hydrothermal recharge, respectively.

Twelve samples, weighing 1.5 g each, were prepared. The experiment was conducted at 150 °C at saturated vapour pressure using Teflon metallic-coated reactors. Details of the experiments are summarised in Fig. 3. Reagent-grade chemicals, including NaCl, $NaHCO_3$ and Na_2S, which contain the most common anions in hydrothermal solutions, were used to prepare the solvents. The chemicals were dried in an oven. Hydrogen peroxide (H_2O_2), at concentrations of ~1.2% by volume, was added to produce oxidising fluids for some experiments. Oxidising fluids are common in hydrothermal environments. A total of 12 experiments were performed. The conditions are shown in Fig. 3 and described below.

3.4.1. Group A

Group A experiments simulated water/rock interaction in solutions that were oxidised, acidic, of medium salinity and contain Cl^-. The duration and W/R ratio varied. Reactor A1 was operated at 150 °C, with a W/R ratio of 26:1, a duration of 15 d, and contained solutions of NaCl synthesised from NaOH powder and pure HCl. Approximately 1.2% hydrogen peroxide solution was added before the vessel was sealed. The pH was adjusted to ~4 by titrating with pure HCl using a pipette. The solvent concentration was ~5 wt% and the solution mass was ~39 g. Reactor A2 was run at a W/R ratio of 13:1 and contained a solution mass of ~19.5 g. The other variables were the same as for reactor A1. Conditions for reactor A3 were similar to those for reactor A1, except for an experimental duration of 30 d. Conditions for reactor A4 were the same as for reactor A2, except that it was run for 30 d.

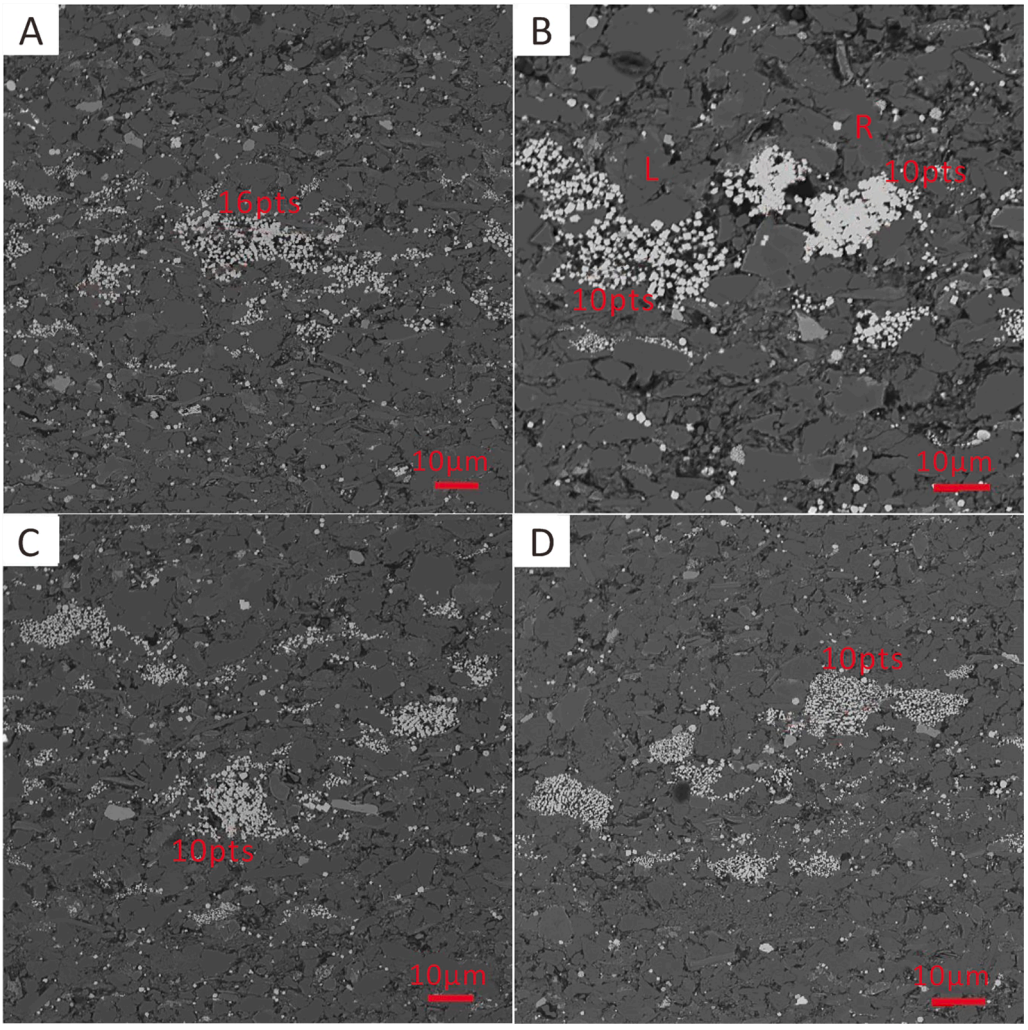

Fig. 4. The BSE images showing the EPMA analysis of pyrite in black shale.

Table 3
EMPA results of pyrites (wt. %) from sample GY31-5.

Type	Au	Ag	As	Sb	Fe	S	Al	Si	S + Fe	Total	S + Fe/Total	S/Fe
Fig. 4A (wt%)	0.039	0.005	0.061	0.005	32.20	40.81	1.21	1.45	73.01	76.87	94.98%	1.27
	0.095	0.019	0.087	0.016	30.80	31.04	0.31	0.42	61.84	65.89	93.85%	1.01
	0	0	0	0.024	18.37	24.24	1.07	1.38	42.61	45.78	93.08%	1.32
	0	0.004	0.008	0.012	26.43	33.14	1.37	1.63	59.56	63.46	93.86%	1.25
	0.007	0.002	0.034	0.017	25.45	26.05	0.94	1.09	51.50	54.39	94.68%	1.02
	0.018	0	0.036	0.012	24.57	27.10	1.07	1.34	51.67	60.52	85.37%	1.10
	0	0	0.046	0.042	33.76	40.51	3.12	4.17	74.27	82.90	89.60%	1.20
	0.027	0.002	0.061	0.039	35.41	41.03	0.94	1.40	76.44	80.14	95.37%	1.16
	0.035	0.011	0.036	0.079	13.95	13.48	3.99	6.73	27.43	39.00	70.33%	0.97
	0.023	0	0.042	0.077	23.51	30.22	3.59	4.39	53.73	62.80	85.55%	1.29
	0.012	0	0.08	0.008	44.90	52.85	0.03	0.11	97.75	99.61	98.13%	1.18
	0.009	0	0.069	0.016	44.29	52.99	0.04	0.14	97.27	99.05	98.21%	1.20
	0.062	0.002	0.069	0.009	24.83	30.78	0.58	0.78	55.61	58.10	95.71%	1.24
	0.035	0.014	0.019	0.007	27.10	34.26	0.26	0.36	61.35	63.04	97.33%	1.26
	0.052	0.004	0.026	0.015	22.10	25.28	0.83	1.09	47.39	50.20	94.40%	1.14
	0.034	0.007	0.029	0.014	18.35	20.59	0.41	0.52	38.94	40.61	95.88%	1.12
Fig. 4BL (wt%)	0	0	0.01	0.117	1.55	0.09	10.34	27.05	1.63	39.58	4.13%	0.06
	0.01	0.004	0.012	0.131	1.23	0.12	9.88	27.67	1.35	39.98	3.38%	0.10
	0.036	0	0.024	0.096	2.22	0.26	10.67	26.54	2.48	40.15	6.17%	0.12
	0.053	0.006	0.013	0.093	4.72	3.80	10.92	22.05	8.52	42.03	20.26%	0.80
	0.022	0.009	0.042	0.11	6.90	6.50	10.30	18.39	13.40	42.70	31.39%	0.94
	0	0	0.012	0.111	26.44	34.02	4.55	7.53	60.46	73.68	82.06%	1.29
	0	0	0.015	0.048	20.14	22.66	1.81	16.00	42.81	61.44	69.67%	1.13
	0.102	0.011	0.021	0.018	12.69	18.68	0.62	25.28	31.37	57.94	54.14%	1.47
	0.051	0	0.024	0.045	21.57	30.54	2.32	12.15	52.11	67.63	77.05%	1.42
	0.071	0.008	0.054	0.032	26.41	29.10	1.91	2.70	55.51	61.22	90.66%	1.10
Fig. 4BR (wt%)	0	0	0.051	0.004	42.97	49.37	0.25	0.42	92.34	94.86	97.34%	1.15
	0	0	0.01	0.015	35.55	45.28	0.59	0.87	80.83	83.65	96.63%	1.27
	0.04	0.012	0.066	0.016	41.30	47.26	0.11	0.27	88.56	90.32	98.05%	1.14
	0.006	0	0.048	0.009	41.10	46.39	0.11	0.23	87.49	89.34	97.93%	1.13
	0	0	0.047	0.015	41.17	47.69	0.25	0.35	88.86	90.92	97.74%	1.16
	0.002	0	0.049	0.013	42.40	49.25	0.11	0.23	91.65	93.32	98.21%	1.16
	0	0	0.078	0.012	44.11	54.79	0.04	0.14	98.90	100.69	98.22%	1.24
	0.003	0.006	0.05	0.016	44.59	53.94	0.06	0.16	98.53	100.31	98.23%	1.21
	0	0.002	0.062	0.013	44.07	52.19	0.06	0.17	96.25	97.99	98.23%	1.18
	0	0.012	0.071	0.01	45.03	54.10	0.01	0.10	99.13	100.83	98.32%	1.20
Fig. 4C (wt%)	0	0.002	0.027	0.012	36.33	39.47	1.65	1.90	75.80	80.51	94.16%	1.09
	0.025	0.003	0.082	0.015	44.56	53.24	0.01	0.08	97.80	99.52	98.26%	1.19
	0	0	0.044	0.019	37.44	41.54	1.40	1.60	78.98	83.28	94.83%	1.11
	0.038	0.006	0.043	0.013	37.46	39.22	1.03	1.32	76.68	80.34	95.44%	1.05
	0.003	0	0.037	0.007	38.60	45.16	1.13	1.51	83.76	87.63	95.59%	1.17
	0	0	0.023	0.016	28.51	31.54	3.98	4.52	60.05	69.45	86.46%	1.11
	0.002	0	0.088	0.018	44.51	52.52	0.03	0.14	97.03	98.85	98.16%	1.18
	0	0	0.045	0.013	39.94	47.22	0.25	0.93	87.16	89.65	97.22%	1.18
	0.008	0.003	0.071	0.014	38.93	46.40	0.41	0.64	85.33	87.91	97.07%	1.19
	0.063	0.009	0.095	0.098	18.34	24.55	5.81	7.83	42.89	57.61	74.45%	1.34
Fig. 4D (wt%)	0	0	0.049	0.051	27.33	28.29	4.49	6.19	55.62	67.44	82.48%	1.03
	0.039	0.002	0.029	0.034	26.81	34.54	1.08	1.80	61.35	65.51	93.65%	1.29
	0	0.001	0.067	0.035	37.56	45.17	1.27	1.99	82.73	87.52	94.53%	1.20
	0	0.003	0.074	0.037	37.28	40.63	0.79	1.35	77.91	81.52	95.57%	1.09
	0	0.002	0.039	0.083	25.66	31.97	3.48	5.30	57.63	67.59	85.27%	1.25
	0.041	0.004	0.022	0.106	25.30	30.79	4.23	5.93	56.09	67.46	83.15%	1.22
	0.026	0.007	0.092	0.044	33.75	37.83	2.64	3.63	71.58	79.30	90.27%	1.12
	0	0	0.069	0.034	37.71	43.01	1.81	2.62	80.73	86.57	93.25%	1.14
	0	0.001	0.028	0.096	19.41	22.59	4.26	11.34	42.00	58.53	71.76%	1.16
	0.109	0.025	0.069	0.046	14.47	19.78	6.59	16.48	34.25	58.60	58.45%	1.37
Average1	0.024	0.005	0.037	0.023	27.88	32.77	1.23	1.69	60.65	65.15	92.27%	1.17
Average2	0.049	0.008	0.023	0.08	12.39	14.58	6.33	18.54	26.96	52.64	43.89%	0.84
Average3	0.013	0.008	0.053	0.012	42.23	50.03	0.16	0.29	92.25	94.22	97.89%	1.19
Average4	0.023	0.005	0.056	0.023	36.46	42.08	1.57	2.05	78.55	83.47	93.16%	1.16
Average5	0.054	0.006	0.054	0.057	28.53	33.46	3.06	5.66	61.99	72.00	84.84%	1.19
Average	0.035	0.007	0.046	0.038	29.32	34.39	2.34	5.22	63.71	72.60	83.47%	1.12

Note: The Average1 represents average value in Fig. 4A; The Average2 represents average value in Fig. 4BL; The Average3 represents average value in Fig. 4BR; The Average4 represents average value in Fig. 4C; The Average5 represents average value in Fig. 4D. The Average represents average value of all pyrites. Fig. 3BL and Fig. 3BR represent the aggregates on the left and right of Fig. 3B, respectively.

3.4.2. Group B

Group B experiments were designed to simulate water/rock interaction in a reducing, weakly alkaline system with moderate concentrations of HS^-. The experiments were performed for different durations and at different W/R ratios. Reactor B1 was run for 15 d at 150 °C with a W/R ratio of 26:1, and contained NaHS synthesised from Na_2S powder and pure HCl. The pH was adjusted to ~8.6 by titrating with pure HCl using a pipette. A pungent odour attributed to H_2S was emitted by the reactors during the experiments, and H_2O_2 solutions were not added because H_2O_2 can oxidise S^{2-} in solution. The solvent concentration was ~5 wt% and the solution mass was ~39 g. Reactor B2 was run with a W/R ratio of 13:1, a solution mass of ~19.5 g and with other variables the same as for reactor B1. Reactor B3 was run for 30 d and other variables the same as for reactor B1. Reactor B4 was run for 30 d and other

Table 4
Leaching rate of Au, Ag, As, and Sb after experiments (ppb for Au and ppm for other elements).

		Au(ppb)			As(ppm)			Ag(ppm)			Sb(ppm)		
		Con1	Con2	Leaching rate	Con1	Con2	Leaching rate	Con1	Con2	Leaching rate	Con1	Con2	Leaching rate
Group A	A1	—	516.46	—	0.00	69.51	0.00%	1.46	3.24	45.20%	0.00	0.00	0.00%
	A2	84.73	516.46	16.40%	0.00	69.51	0.00%	1.19	3.24	36.81%	0.00	0.00	0.00%
	A3	83.60	516.46	16.19%	0.00	69.51	0.00%	1.19	3.24	36.79%	0.00	0.00	0.00%
	A4	30.80	516.46	5.96%	0.00	69.51	0.00%	1.07	3.24	33.19%	0.00	0.00	0.00%
Group B	B1	31.28	516.46	6.06%	3.13	69.51	4.50%	0.00	3.24	0.00%	0.00	0.00	0.00%
	B2	13.56	516.46	2.63%	0.00	69.51	0.00%	0.00	3.24	0.00%	0.00	0.00	0.00%
	B3	25.11	516.46	4.86%	15.75	69.51	22.66%	0.00	3.24	0.00%	0.00	0.00	0.00%
	B4	12.85	516.46	2.49%	0.00	69.51	0.00%	0.00	3.24	0.00%	0.00	0.00	0.00%
Group C	C1	18.95	516.46	3.67%	4.54	69.51	6.54%	0.74	3.24	22.84%	0.00	0.00	0.00%
	C2	1.89	516.46	0.37%	0.00	69.51	0.00%	0.52	3.24	15.80%	0.00	0.00	0.00%
	C3	3.94	516.46	0.76%	7.25	69.51	10.42%	0.58	3.24	17.97%	0.00	0.00	0.00%
	C4	1.78	516.46	0.35%	0.00	69.51	0.00%	0.42	3.24	12.86%	0.00	0.00	0.00%

Note: Con1 represents the content of element in the solutions after experiment; Con2 represents the content of element of whole rock for each sample (1.5 g); Leaching rate is equal to the value of Con1/Con2.

variables the same as for reactor B2.

3.4.3. Group C

Group C experiments were designed to simulate water/rock interaction in an oxidised, weakly alkaline system containing medium concentrations of HCO_3^-. The duration and W/R ratio varied. Reactor C1 was run for 15 d at 150 °C with a W/R ratio of 26:1 and contained a solution of $NaHCO_3$ synthesised from pure $NaHCO_3$ powder. Approximately 1.2% H_2O_2 solution was added. The pH was set to ~9.2 by titrating with pure HCl using a pipette. The solvent concentration was ~5 wt% and the solution mass was ~39 g. Reactor C2 was run with a W/R ratio of 13:1, a solution mass of ~19.5 g and other variables were the same as for reactor C1. Reactor C3 was run for 30 d and other variables were the same as for reactor C1. Reactor C4 was run for 30 days and other variables were the same as for reactor C2.

After the experiments, the solids and liquids from all reactors were separated by centrifugation at 4000 rpm. The pH of the supernatant was determined (Table 2). The supernatant in groups A and C were transparent, and pale yellow in Group B, reflecting oxidation of S^{2-}. One mL of supernatant was added to 1 mL of pure concentrated HNO_3, and diluted to 50 mL with deionised water for trace element analysis.

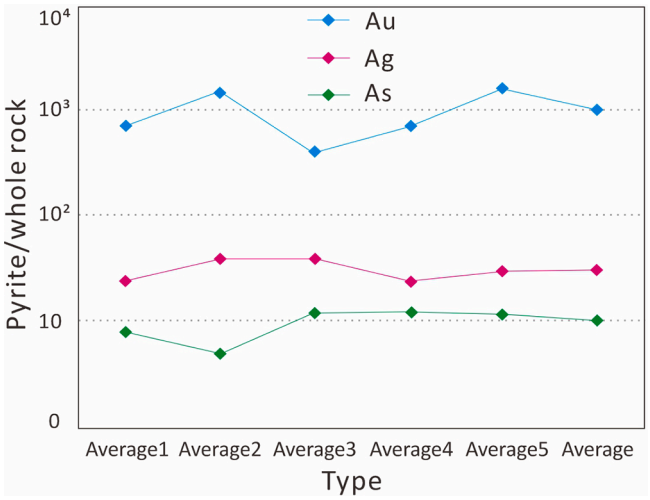

Fig. 5. Coefficients (pyrite/black shale) of average concentration of Au, Ag, and As in different kinds of pyrite aggregates.

4. Results

4.1. Electron microprobe and scanning electron microscope results

The EPMA results and SEM images show that pyrite is the only mineral containing detectable amounts of Au (Figs. 2 and 4). The SEM images show two pyrite forms: (1) Irregular grains, a few micrometres to tens of micrometres in size. These pyrite grains are corroded and recrystallised; (2) Micrometre-sized rounded framboidal pyrite. Some grains are isolated and rounded, and some form spherical clusters of framboids.

To determine the distribution of trace elements in pyrite, point analyses were performed on a traverse across pyrite aggregates (Fig. 4; Table 3). The maximum Au concentration is 0.109 wt% (Fig. 4D; Table 3), with an average value of 0.035 wt%. The maximum Ag content of pyrite is 0.025 wt% with an average value of 0.007 wt%. The maximum As content is 0.095 wt% with an average value of 0.046 wt%. The maximum Sb content is 0.131 wt% with an average value of 0.038 wt%.

4.2. Leaching results

The proportions of trace elements leached by the experiments are shown in Table 4. For Au, leaching from Group A experiments (oxidised acidic systems containing HCO_3^-) ranged from 5.96% to 16.40%. The proportion of Au leached from Group B experiments (reducing weakly alkaline systems containing HS^-) ranged from 6.06% to 2.49%. The proportion of Au leached from Group C experiments (oxidised weakly alkaline systems) was the smallest, and ranged from <1% to 3.67%.

There was almost no leaching of Ag from the Group B experiments; this is attributed to the formation of Ag_2S, which has a lower solubility than AgCl. The proportion of Ag leached from the Group A experiments ranged from 33.19% to 45.20%, and the proportion of Ag leached from the Group C experiments typically ranged from 12.86% to 22.84%. Little As was leached during the Group A experiments and As leaching was more effective from groups B and C. Leaching of Sb was not observed for any of the experiments. In summary, Au and Ag were leached more effectively than the other elements investigated.

5. Discussion

5.1. Occurrence of trace elements in black shale

The experimental results indicate that a range of factors affect trace element leaching, and that the form of the trace element host is influential. Pyrite commonly contains a range of trace elements (Sung et al., 2009; Schindler et al., 2016; Zhai et al., 2018). In the present study, Au, Ag and As are enriched in pyrite relative to the black shale whole-rock composition. The Au enrichment coefficients of the five aggregates (Fig. 4; Table 3) are 697, 1423, 378, 668 and 1568, respectively, with an average enrichment coefficient of 1000 (Fig. 5). The Ag-enrichment coefficients for the five aggregates are 23, 37, 37, 23 and 28,

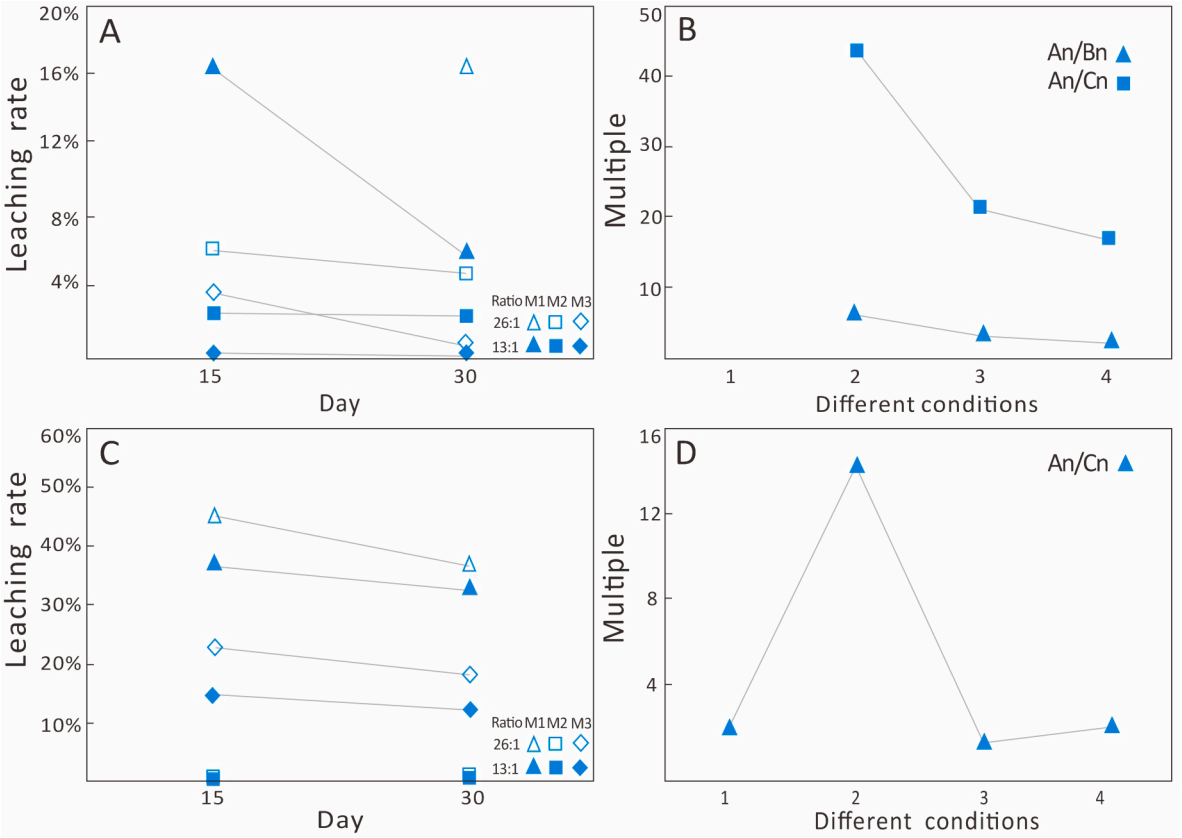

Fig. 6. (A) Line chart of leaching rate of Au. (B) Ratio of An/Bn and An/Cn for Au in the same conditions but different mediums. (C) Line chart of leaching rate of Ag. (D) Ratio of An/Cn for Ag in the same conditions but different mediums.

Table 5
Ratio of leaching rate of sample GY31-5 in different W/R for Au.

W/R	A1/A2	A3/A4	B1/B2	B3/B4	C1/C2	C3/C4
Ratio	—	2.7	2.3	2.0	9.92	2.2

respectively, with an average enrichment coefficient of 29.6 (Fig. 5). The As-enrichment coefficients are 8, 5, 11, 12 and 12, respectively, with an average enrichment coefficient of 10. The high value of the enrichment coefficients indicates that most of the Au, Ag and As within the black shale is contained by pyrite.

5.2. Leaching of Au and Ag

The experimental results show that Au was leached most effectively from the Cl^--bearing Group A experiments, and least effectively by Group C experiments (Fig. 6A). We calculated ratios for leaching from the different experiments to compare leaching under similar conditions, but in different media (Fig. 6B). These ratios indicate that leaching from Group A experiments is 2.4–6 times more effective than leaching from Group B experiments. Leaching from Group A experiments was 17–44 times more effective than leaching from Group C experiments. In addition, dissolved Au might have reprecipitated in the reducing environment of the Group B experiments in the form of elemental Au, and this might have contributed to the low effectiveness of leaching for Group B. The proportion of Ag leached from Group A experiments was higher than that leached from Group B and Group C experiments (Fig. 6C), and leaching from Group A experiments was 2–14 times more effective than leaching from Group C experiments (Fig. 6D). In summary, leaching of Au and Ag is more effective in Cl^--bearing oxidised acidic systems than in HS-bearing, reducing, weakly alkaline systems or HCO_3^--bearing oxidised alkaline systems. Ag-leaching from the HS^--bearing system was negligible.

The rate of Au- and Ag-leaching decreased with time (Fig. 6A). This might indicate that fluid-rock interaction altered the composition of the fluid such that leaching rates decreased. Au- and Ag-leaching was most effective at a high W/R ratio (Table 5); indicating that a relatively open system with more hydrothermal recharge favours metal leaching.

5.3. Influence of organic material

Previous studies have found an inverse relationship between organic matter and Au content in the solution (Wang, 1998; Xing et al., 2018). Some organic ligands can displace Cl^- ions from Au-chloride complexes to precipitate Au-organic compounds (Radtke and Scheiner, 1970). Organic carbon can also adsorb Au-complexes efficiently from solution (Liu et al., 1984). Black shales are enriched in organic matter, and this might have suppressed Au-leaching in our experiments. Moreover, the decrease in leaching rate with time might be related to organic matter (Fig. 6A and C).

5.4. Implications for low-temperature mineralisation

Black shales provide strongly reducing environments, and a range of metals, alloys, and intermetallic compounds are enriched in mineralised black shales (Distler and Yudovskaya, 2001). Ore-forming elements, particularly Au, can occur in pyrite as nanoparticles. Moreover, gold can occur as structurally-bound $Au^{\pm}$ colloid complexes, under some conditions, and these can be transported by hydrothermal fluids (Reich et al., 2005; Etschmann et al., 2017; Cumberland et al., 2018). Anions such as Cl^-, HS^- and HCO_3^- are common in hydrothermal fluids and can complex with Au and other chalcophile cations (Su et al., 2012). Some trace elements found in pyrite form complexes with these anions; common

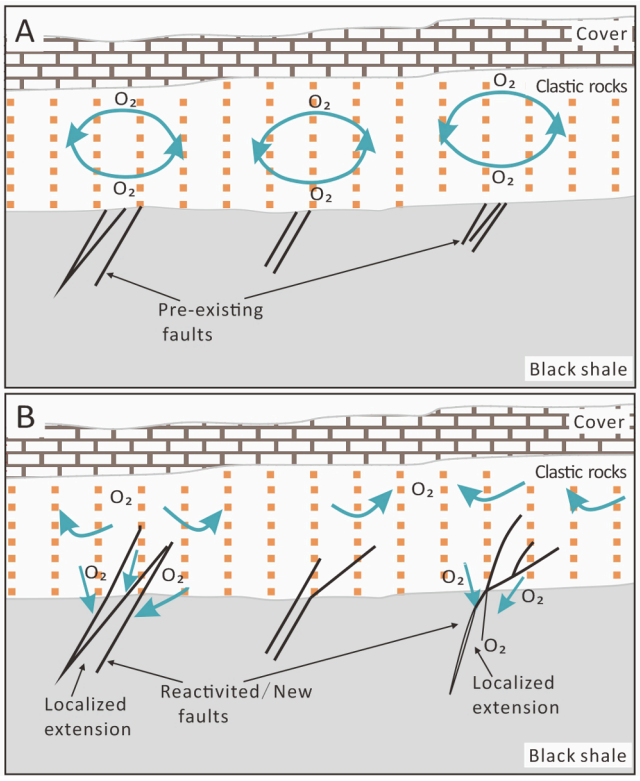

Fig. 7. A sketch genetic model that the black shale were leached by hydrothermal solution (modified after Cui et al., 2012). Arrows indicate fluid flow directions. (A) Free convection forms in the clastic sequence when the tectonics is quiescent. (B) The leaching process occurred between black shale and hydrothermal solution when the extensional deformation occurs.

Au-bearing complexes include $AuCl_2^-$, $Au(HS)_2^-$ and $Au(HCO_3)_2^-$.

Solute-bearing hydrothermal fluids might have mobilised and transported trace elements during the formation of large-scale, low-temperature mineralisation within the South China Block. Thermally driven convection could be favoured by tectonic setting, such as extension setting (Oliver et al., 2006). However, numerical modeling of fluid flow indicate that thermally driven convection might also occur in sandstone units without tectonic activity (Cui et al., 2012; Dong et al., 2016), and this might transport dissolved oxygen from shallow to deep parts of the crust. Alternatively, convection can occur in other clastic rocks with relatively high porosity (Fig. 7A). Tectonic activity reactivates basement structures and generates new faults, joints and fractures. High strain rates inhibited preexisting thermally driven free convection and facilitated deformation-dominated fluid flow or mixed convection (Cui et al., 2012). Black shales are leached most effectively in intensively-deformed structural settings, such as fold hinge zones or ductile shear zones. Deep-seated magma formed during the Indosinian and Yanshanian tectonic events (Qiu et al., 2015, 2016, 2017; Chen et al., 2016; Hu et al., 2016; Pi et al., 2016; Zhu et al., 2016), and was associated with flow of oxidised acidic hydrothermal fluids containing Cl^- or other anions into extensional sites within the black shales (i.e., faults, joints and fractures; Fig. 7B). In these settings, multiple cycles of fluid-rock interaction leached trace elements into hydrothermal fluids that migrated towards sites favourable for mineralisation along faults and fractures that formed at different times during the evolution of this area.

6. Conclusions

The following conclusions are based on our experimental investigation of fluid-rock interaction:

(1) Au- and Ag-leaching are more effective in oxidised acidic Cl^--bearing systems than in reducing weakly alkaline HS^--bearing systems or oxidised alkaline HCO_3^--bearing systems. Ag-leaching from the HS^--bearing system was negligible.

(2) The EPMA results show that Au, Ag and As are enriched in pyrite relative to the whole rock. Therefore, pyrite is the main source of Au, Ag and As in black shale.

(3) The experiments provide support for a conceptual model that describes the mobilisation and transport of ore-forming elements, particularly Au and Ag.

Declaration of Competing Interest

The authors declare that they have no known competing financial interests or personal relationships that could have appeared to influence the work reported in this paper.

Acknowledgments

The research is supported by NSFC (grants 42030306, 41972206 and 41702207), the National Basic Research Program of China (973 Program, grants 2014CB440903) and the Fundamental Research Funds for the Central Universities (grant 2652019046). We thank Lin Li, Tao Jin and Wang Ma for valuable discussions and Qiangmao Wang, Yuyan Shi and Kuo Wang for their help with the manuscript.

References

Anjum, F., Bhatti, H.N., Asgher, M., Shahid, M., 2010. Leaching of metal ions from black shale by organic acids produced by Aspergillus niger. Appl. Clay. Sci. 47, 356–361.
Barnes, H.L., 1979. Solubilities of ore minerals. Geochem. Hydroth. Ore Depos. 404–460.
Chen, X., Su, W.C., Huang, Y., 2016. He and Ar isotope geochemistry of ore-forming fluids for the Qinglong Sb deposit in Guizhou Province China. Acta. Petrol. Sin. 32 (11), 3312–3320 (in Chinese with English abstract).
Chen, Y.Q., Jiang, S.Y., Ling, H.F., Feng, H.Z., Yang, J.H., Chen, J.H., 2003. Pb-Pb isotope dating of black shales from the Lower Cambrian Niutitang formation, Guizhou Province, south China. Prog. Nat. Sci. 13 (10), 771–776.
Cui, T., Yang, J.W., Samson, I.M., 2012. Tectonic deformation and fluid flow: implications for the formation of unconformity-related uranium deposits. Econ. Geol. 107 (1), 147–163.
Cumberland, S.A., Etschmann, B., Brugger, J., Douglas, G., Evans, K., Fisher, L., Kappen, P., Moreau, J.W., 2018. Characterization of uranium redox state in organic-rich Eocene sediments. Chemosphere 194, 602–613.
Deng, X., Yang, K.G., Liu, Y.L., 2010. Characteristics and tectonic evolution of Qianzhong uplift. Earth Sci. Front. 17 (3), 79–89 (in Chinese with English abstract).
Distler, V.V., Yudovskaya, M.A., 2001. Genetic Model of the Black Shale Hosted PGE-Gold Sukhoi Log Deposit (Russia). In: Mineral Deposits at the Beginning of the 21st Century, pp. 151–153.
Dong, W.D., Shen, N.P., Su, W.C., Cai, J.L., 2016. Study on the ore-forming fluid geochemistry of the Anna gold deposit in southeastern Yunnan Province. China. Acta. Petrol. Sin. 32 (11), 3321–3330 (in Chinese with English abstract).
Etschmann, B., Liu, W., Li, K., Dai, S., Reith, F., Falconer, D., Kerr, G., Paterson, D., Howard, D., Kappen, P., 2017. Enrichment of germanium and associated arsenic and tungsten in coal and roll-front uranium deposits. Chem. Geol. 463, 29–49.
Falk, H., Lavergren, U., Bergbäck, B., 2006. Metal mobility in alum shale from Öland Sweden. J. Geochem. Explor. 90, 157–165.
Gao, Z.M., Luo, T.Y., Li, S.R., 1997. The origin of metal-enriched layer in the black rock series. Geol. Geochem. 1, 18–23 (in Chinese with English abstract).
Gu, X.X., Zhang, Y.M., Li, B.H., Dong, S.Y., Xue, C.J., Fu, S.H., 2012. Hydrocarbon-and ore-bearing basinal fluids: a possible link between gold mineralization and hydrocarbon accumulation in the Youjiang basin South China. Miner. Depos. 47 (6), 663–682.
Hu, R.Z., Su, W.C., Bi, X.W., Tu, G.Z., Hofstra, A.H., 2002. Geology and geochemistry of Carlin-type gold deposits in China. Miner. Depos. 37, 378–392.
Hu, R.Z., Peng, J.T., Ma, D.S., 2007. Epoch of large-scale low-temperature mineralizations in southwestern Yangtze massif. Miner. Depos. 26, 583–596 (in Chinese with English abstract).
Hu, R.Z., Zhou, M.F., 2012. Multiple Mesozoic mineralization events in South China-an introduction to the thematic issue. Miner. Depos. 47 (6), 579–588.
Hu, R.Z., Fu, S.L., Xiao, J.F., 2016. Major scientific problems on low-temperature metallogenesis in South China. Acta. Petrol. Sin. 32, 3239–3251 (in Chinese with English abstract).
Kwong, Y.J., Whitley, G., Roach, P., 2009. Natural acid rock drainage associated with black shale in the Yukon Territory Canada. Appl. Geochem. 24 (2), 221–231.
Lehmann, B., Frei, R., Xu, L.G., Mao, J.W., 2016. Early Cambrian black shale-hosted Mo-Ni and V mineralization on the rifted margin of the Yangtze Platform, China:

reconnaissance chromium isotope data and a refined metallogenic model. Econ. Geol. 111 (1), 89–103.
Li, C.Y., 1999. Some geological characteristics of concentrated distribution area of epithermal deposits in China. Earth Sci. Front. 6 (1), 163–170 (in Chinese with English abstract).
Li, C.X., Wei, C., Deng, Z.G., Li, M.T., Li, X.B., Fan, G., 2010. Recovery of vanadium from black shale. T. Nonferr. Metal. Soc. 20, 127–131.
Liu, J.J., Yang, D., Liu, J.M., Liu, Z.J., Zheng, M.H., 2007. Mineralogical characteristics of native arsenic and tracing the metallogenic physicochemical condition in Carlin-type gold deposits. Earth Sci. Front. 14 (5), 158–166.
Liu, J.J., Dai, H.Z., Zhai, D.G., Wang, J.P., Wang, Y.H., Yang, L.B., 2015. Geological and geochemical characteristics and formation mechanisms of the Zhaishang Carlin-like type gold deposit, western Qinling Mountains China. Ore. Geol. Rev. 64, 273–298.
Liu, S.H., Hinnen, C., Van Huong, C.N., De Tacconi, N.R., Ho, K.M., 1984. Surface state effects on the electroreflectance spectroscopy of Au single crystal surfaces. J. Electroanal. Chem. Interfacial Electrochem. 176 (1–2), 325–338.
Liu, S.F., Steel, R., Zhang, G.W., 2005. Mesozoic sedimentary basin development and tectonic implication, northern Yangtze Block, eastern China: record of continent-continent collision. J. Asian. Earth. Sci. 25 (1), 9–27.
Liu, Y.Z., Xiao, T.F., Perkins, R.B., Zhu, J.M., Zhu, Z.J., Xiong, Y., Ning, Z.P., 2017. Geogenic cadmium pollution and potential health risks, with emphasis on black shale. J. Geochem. Explor. 176, 42–49.
Mao, J.W., 2001. The study of deposits related to the black shale series. Miner. Depos. 20 (4), 402–403 (in Chinese).
Mao, J.W., Lehmann, B., Du, A., Zhang, G., Ma, D., Wang, Y., Kerrich, R., 2002. Re-Os dating of polymetallic Ni-Mo-PGE-Au mineralization in Lower Cambrian black shales of South China and its geologic significance. Econ. Geol. 97 (5), 1051–1061.
Matlakowska, R., Sklodowska, A., 2011. Biodegradation of Kupferschiefer black shale organic matter (Fore-Sudetic Monocline, Poland) by indigenous microorganisms. Chemosphere 83 (9), 1255–1261.
Muntean, J.L., Cline, J.S., Simon, A.C., Longo, A.A., 2011. Magmatic-hydrothermal origin of Nevada's Carlin-type gold deposits. Nat. Geosci. 4, 122–127.
Ogawa, Y., Shikazono, N., Ishiyama, D., Sato, H., Mizuta, T., 2005. An experimental study on felsic rock-artificial seawater interaction: implications for hydrothermal alteration and sulfate formation in the Kuroko mining area of Japan. Miner. Depos. 39 (8), 813–821.
Oliver, N.H., McLellan, J.G., Hobbs, B.E., Cleverly, J.S., Ord, A., Feltrin, L., 2006. Numerical models of extensional deformation, heat transfer, and fluid flow across basement-cover interfaces during basin-related mineralization. Econ. Geol. 101 (1), 1–31.
Pi, Q.H., Hu, R.Z., Peng, K.Q., Wu, J.B., Wei, Z.W., Huang, Y., 2016. Geochronology of the Zhesang gold deposit and mafic rock in Funing County of Yunnan Province, with special reference to the dynamic background of Carlin-type gold deposits in the Dian-Qian-Gui region. Acta. Petrol. Sin. 32 (11), 3331–3342 (in Chinese with English abstract).
Qi, L., Zhou, M.F., 2008. Platinum-group elemental and Sr-Nd-Os isotopic geochemistry of Permian Emeishan flood basalts in Guizhou Province, SW china. Chem. Geol. 248, 83–103.
Qiu, L., Yan, D.P., Zhou, M.F., Gao, J.F., Tang, S.L., Barnes, M., 2015. Geochemistry and U-Pb zircon age of Late Triassic volcanogenic sediments in the central Yangtze Block: Origin and tectonic implications. J. Miner. Geochem. 192, 211–227.
Qiu, L., Yan, D.P., Tang, S.L., Wang, Q., Yang, W.X., Tang, X., Wang, J., 2016. Mesozoic geology of southwestern China: Indosinian foreland overthrusting and subsequent deformation. J. Asian. Earth. Sci. 122, 91–105.
Qiu, L., Yan, D.P., Yang, W.X., Wang, J.B., Tang, X.L., Ariser, S., 2017. Early to Middle Triassic sedimentary records in the Youjiang Basin, south China: implications for Indosinian orogenesis. J. Asian. Earth. Sci. 141, 125–139.
Qiu, L., Yang, W.X., Yan, D.P., Wells, M.L., Qiu, J.T., Gao, T., Dong, J.M., Zhang, L., Wang, F.Y., 2019. Geochronology of early Mesozoic diabase units in southwestern China: metallogenic and tectonic implications. Geol. Mag. 156 (7), 1141–1156.
Radtke, A.S., Scheiner, B.J., 1970. Studies of hydrothermal gold deposition (1) Carlin gold deposit, Nevada, the role of carbonaceous materials in gold deposition. Econ. Geol. 65 (2), 87–102.
Reich, M., Kesler, S.E., Utsunomiya, S., Palenik, C.S., Chryssoulis, S.L., Ewing, R.C., 2005. Solubility of gold in arsenian pyrite. Geochim. Cosmochim. Ac. 69 (11), 2781–2796.
Robinson, P.T., Zhou, M.F., 2008. The origin and tectonic setting of ophiolites in China. J. Asian. Earth. Sci. 32 (5), 301–307.
Roedder, E., 1984. Fluid-inclusion evidence bearing on the environments of gold deposition. In Gold'82: the geology, geochemistry and genesis of gold deposits. In: Symposium, pp. 129–163.
Schindler, C., Hagemann, S.G., Banks, D., Mernagh, T., Harris, A.C., 2016. Magmatic Hydrothermal Fluids at the Sedimentary Rock-Hosted, Intrusion-Related Telfer Gold-Copper Deposit, Paterson Orogen, Western Australia: PressureTemperature-Composition Constraints on the Ore-Forming Fluids. Econ. Geol. 111, 1099–1126.
Song, Z.D., Qiu, L., Zhang, Y., 2017. The Paleozoic deformational characteristics and tectonic significance of the Weng'an Dome in the Southwest Yangtze Block. Earth Sci. Front. 24 (5).
Su, W.C., Heinrich, C.A., Pettke, T., Zhang, X.C., Hu, R.Z., Xia, B., 2009. Sediment-hosted gold deposits in Guizhou, China: products of wall-rock sulfidation by deep crustal fluids. Econ. Geol. 104 (1), 73–93.
Su, W.C., Zhang, H.T., Hu, R.Z., Ge, X., Xia, B., Chen, Y.Y., Zhu, C., 2012. Mineralogy and geochemistry of gold-bearing arsenian pyrite from the Shuiyindong Carlin-type gold deposit, Guizhou, China: implications for gold depositional processes. Miner. Depos. 47 (6), 653–662.
Sung, Y.H., Brugger, J., Ciobanu, C.L., Pring, A., Skinner, W., Nugus, M., 2009. Invisible gold in arsenian pyrite and arsenopyrite from a multistage Archaean gold deposit: Sunrise Dam, Eastern Goldfields Province, Western Australia. Miner. Depos. 44, 765–791.
Tu, G.C., 2002. Two unique mineralization areas in Southwest China. Bull. Miner. Petrol. Geochem. 21 (1), 1–2 (in Chinese with English abstract).
Wang, W., Zhou, M.F., Yan, D.P., Li, J.W., 2012. Depositional age, provenance, and tectonic setting of the Neoproterozoic Sibao Group, southeastern Yangtze Block, South China. Precam. Res. 192, 107–124.
Wang, X.Q., 1998. Leaching of mobile forms of metals in overburden: development and application. J. Geochem. Explor. 61, 39–55.
Wang, Y.J., Fan, W.M., Zhang, G.W., Zhang, Y.H., 2013. Phanerozoic tectonics of the South China Block: key observations and controversies. Gondwana. Res. 23 (4), 1273–1305.
Watling, H.R., Collinson, D.M., Watling, R.J., Shiers, D.W., 2017. Simulated heap leaching and recovery of multiple elements from a mineralised black shale. Hydrometallurgy 167, 48–57.
Wu, S.Y., Hou, L., Ding, J., Wu, W., Qin, K., Zhang, J.R., Zhu, S.B., 2016. Ore-controlling structure types and characteristics of ore-forming fluid of the Carlin-type gold orefield in southwestern Guizhou. China. Acta. Petrol. Sin. 32 (8), 2407–2424 (in Chinese with English abstract).
Xing, W.D., Lee, M.S., Senanayake, G., 2018. Recovery of metals from chloride leach solutions of anode slimes by solvent extraction. Part I: recovery of gold with Cyanex 272. Hydrometallurgy 180, 58–64.
Xu, L.G., Lehmann, B., Mao, J.W., Qu, W.J., Du, A.D., 2011. Re-os age of polymetallic ni-mo-pge-au mineralization in early cambrian black shales of south china — a reassessment. Econ. Geol. 106 (3), 511–522.
Xu, L.G., Lehmann, B., Mao, J.W., 2013. Seawater contribution to polymetallic Ni-Mo-PGE-Au mineralization in Early Cambrian black shales of South China: evidence from Mo isotope, PGE, trace element, and REE geochemistry. Ore. Geol. Rev. 52, 66–84.
Yan, D.P., Zhou, M.F., Wang, C.Y., Xia, B., 2006. Structural and geochronological constraints on the tectonic evolution of the Dulong-Song Chay tectonic dome in Yunnan province SW China. J. Asian. Earth. Sci. 28 (4), 332–353.
Yan, D.P., Zhou, M.F., Wei, G.Q., Gao, J.F., Liu, S.F., Xu, P., Shi, X.Y., 2008. The Pengguan tectonic dome of Longmen Mountains, Sichuan Province: Mesozoic denudation of a Neoproterozoic magmatic arc-basin system. Sci. China. Ser. D. 51 (11), 1545–1559.
Yan, D.P., Zhang, B., Zhou, M.F., Wei, G., Song, H.L., Liu, S.F., 2009. Constraints on the depth, geometry and kinematics of blind detachment faults provided by fault-propagation folds: an example from the Mesozoic fold belt of South China. J. Struct. Geol. 31 (2), 150–162.
Yan, D.P., Zhou, M.F., Zhao, D., Li, J.W., Wang, G.H., Wang, C.L., Qi, L., 2011. Origin, ascent and oblique emplacement of magmas in a thickened crust: an example from the Cretaceous Fangshan adakitic pluton Beijing. Lithos. 123, 102–120.
Yang, J., Yi, F.C., Li, H.J., Hou, L.J., 2004. Genesis and petrogeochemistry characteristics of Lower Cambrian black shale series in northern Guizhou. Acta Miner. Sin. 24 (3), 285–289 (in Chinese with English abstract).
Yang, X.L., Zhu, M.Y., Zhao, Y.L., Zhang, J.M., Guo, Q.J., Li, B.X., 2007. Trace element geochemical characteristics from the Ediacaran-Cambrian transition duration in Eastern Guizhou South China. Acta Geol. Sin. 81 (10), 1391–1397 (in Chinese with English abstract).
Yin, R.S., Xu, L.G., Lehmann, B., Lepak, R.F., Hurley, J.P., Mao, J.W., Feng, X.B., Hu, R. Z., 2017. Anomalous mercury enrichment in early cambrian black shales of south china: mercury isotopes indicate a seawater source. Chem. Geol. 467, 159–167.
Yu, C.X., Peng, B., Peltola, P., Tang, X.Y., Xie, S.R., 2012. Effect of weathering on abundance and release of potentially toxic elements in soils developed on Lower Cambrian black shales PR China. Environ. Geochem. Hlth. 34 (3), 375–390.
Yu, C.X., Lavergren, U., Peltola, P., Drake, H., Bergbäck, B., Åström, M.E., 2014. Retention and transport of arsenic, uranium and nickel in a black shale setting revealed by a long-term humidity cell test and sequential chemical extractions. Chem. Geol. 363, 134–144.
Zhai, D.G., Williams-Jones, A.E., Liu, J.J., Tombros, S.F., Cook, N.J., 2018. Mineralogical, fluid inclusion, and multiple isotope (H-O-S-Pb) constraints on the genesis of the Sandaowanzi epithermal Au-Ag-Te deposit, NE China. Econ. Geol. 113, 1359–1382.
Zhang, K.J., Cai, J.X., Zhu, J.X., 2006. North China and South China collision: insights from analogue modeling. J. Geodyn. 42 (1), 38–51.
Zhang, Y., Yan, D.P., Zhao, F., Li, X.T., Qiu, L., Zhang, Y.X., 2016. Stratigraphic sequences, abundance anomalies and occurrences of As, Sb, Au, Ag in the Lower Cambrian Niutitang Formation in Kaiyang Phosphate Mine area. Acta. Petrol. Sin. 32 (11), 3252–3268 (in Chinese with English abstract).
Zhao, Z.H., Tu, G.C., 2003. Super Ore Deposits in China (II). Science Press, Beijing (in Chinese).
Zhou, J.X., Huang, Z.L., Zhou, M.F., Zhu, X.K., Muchez, P., 2014. Zinc, sulfur and lead isotopic variations in carbonate-hosted Pb-Zn sulfide deposits, Southwest China. Ore. Geol. Rev. 58, 41–54.
Zhou, M.F., Yan, D.P., Vasconcelos, P.M., Li, J.W., Hu, R.Z., 2008. Structural and geochronological constraints on the tectono-thermal evolution of the Danba domal terrane, eastern margin of the Tibetan plateau. J. Asian. Earth. Sci. 33 (5), 414–427.
Zhu, J.J., Zhong, H., Xie, G.Q., Zhao, C.H., Xu, L.L., Lu, G., 2016. Origin and geological implication of the inherited zircon from felsic dykes, Youjiang basin China. Acta. Petrol. Sin. 32 (11), 3269–3280 (in Chinese with English abstract).